



Meridional oscillation in genesis location of tropical cyclones in the postmonsoon Bay of Bengal

Kaigui Fan¹ · Xidong Wang^{1,2} · Gregory R. Foltz³ · Karthik Balaguru⁴

Received: 11 December 2018 / Accepted: 29 April 2019
© Springer-Verlag GmbH Germany, part of Springer Nature 2019

Abstract

It is found that the average genesis location of tropical cyclones (TCs) in the postmonsoon (October–December) Bay of Bengal (BoB) shows a notable meridional oscillation during 1980–2015. During years when the average genesis location shifts northward (north-years), the average maximum sustained wind speed, the average landfall wind speed and the number of category 4–5 TCs are all larger than those during years when the average genesis location displaces southward (south-years). Genesis potential index analysis shows that changes in relative humidity and vertical wind shear are mainly responsible for the meridional oscillation of the average genesis location of TCs. The changes in relative humidity and wind shear are closely related to changes in atmospheric circulation. Composite analysis reveals that sea surface temperature (SST) anomalies over the equatorial Pacific Ocean show a La Niña-like pattern (El Niño-like pattern) during north-years (south-years) of TC genesis locations. The SST anomalies over the equatorial Pacific Ocean induce a strengthened (weakened) Walker circulation during north-years (south-years) of TC genesis locations, influencing the atmospheric circulation over the tropical Indian Ocean. In addition, a stationary Rossby wave train from the North Pacific to the Iranian Plateau (east of Iranian Plateau) during north-years (south-years) induces changes in atmospheric circulation over the extratropical North Indian Ocean. Together, the tropical and extratropical influences contribute to the north–south patterns of relative humidity and vertical wind shear anomalies in the postmonsoon BoB, which drive the meridional oscillation of TC genesis locations. This study has significant implications for the prediction of TCs and disaster prevention and mitigation over the BoB.

Keywords Bay of Bengal · Tropical cyclone · El Niño–Southern Oscillation · Pacific Decadal Oscillation

1 Introduction

Tropical cyclones (TCs), driven mainly by heat transfer from the tropical oceans, are among the deadliest weather systems in nature (Emanuel 2003). The North Indian Ocean (NIO), including the Bay of Bengal (BoB) and Arabian Sea, is one of the warm pools conducive to TC formation and home to

about 7% of global TCs annually (Gray 1985). TC frequency is higher in the BoB than in the Arabian Sea, with the BoB accounting for approximately two-thirds of TCs in the NIO (Li et al. 2013). Although fewer TCs form in the BoB than in the Pacific and Atlantic Oceans, the most devastating losses of lives and property from TCs occur in the BoB due to the low flat coastal terrain, shallow waters, funnel shape of the coastline (McBride 1995) and the high population density along the coast. In the past 300 years, more than 75% of global TCs causing 5000 or more human deaths have occurred over the NIO (Mohanty et al. 2013).

Due to the migration of the monsoon trough and changes in vertical wind shear, most TCs in the BoB form in the pre-monsoon and postmonsoon seasons, whereas few TCs occur during the mature monsoon phase. Thus, TC frequency in the BoB exhibits a notable bimodal distribution (Alam et al. 2003; Yanase et al. 2012). There is more frequent TC genesis in the postmonsoon season because of the higher background relative humidity (Li et al. 2013).

✉ Xidong Wang
xidong_wang@hhu.edu.cn

¹ College of Oceanography, Hohai University, Nanjing 210098, China

² Laboratory for Regional Oceanography and Numerical Modeling, Qingdao National Laboratory for Marine Science and Technology, Qingdao 266237, China

³ Atlantic Oceanographic and Meteorological Laboratory, Miami, FL, USA

⁴ Marine Sciences Laboratory, Pacific Northwest National Laboratory, Seattle, WA, USA

A study has suggested that the frequency of TCs has decreased globally, while the intensity of TCs has increased in the NIO with the increasing of sea surface temperature (SST) (Webster et al. 2005). Wang et al. (2013) found that TCs have intensified over the BoB in May after 1979 due to a deepening of the monsoon trough and tropospheric warming, which can possibly be attributed to aerosols and greenhouse gases. Balaguru et al. (2016) noted that TC intensification rates increased in the northern BoB and decreased in the southern BoB for the months of May–June during 1979–2014, owing to a strengthening of the monsoon circulation induced by El Niño–Southern Oscillation (ENSO). Balaguru et al. (2014) found that the intensity of BoB TCs also increased in the months of October and November during 1980–2010 and demonstrated that changes in large-scale environmental factors caused the increases in TC intensity.

Previous studies have focused on interannual and interdecadal variations of TC activity in the BoB. For the post-monsoon BoB, they have found that there are more extreme TCs (wind speed > 64 knots) during La Niña events than El Niño events. The Madden–Julian Oscillation (MJO) shows differences between El Niño and La Niña events, and these differences exert a significant influence on TC formation (Girishkumar and Ravichandran 2012). Felton et al. (2013) also found that ENSO modulates TC activity over the BoB and suggested that the combination of low-level cyclonic vorticity, weak vertical wind shear, and enhanced relative humidity favor TC genesis during La Niña events. A recent study found that the Pacific Decadal Oscillation (PDO) affects the relationship between ENSO and TC activity in the postmonsoon BoB. During the warm phase of the PDO, there are more TCs and intense TCs (wind speed > 64 knots) during La Niña events than during El Niño events. However, there are no significant differences under the cold phase of the PDO (Girishkumar et al. 2014b).

A study by Balaji et al. (2018) showed that the average genesis location of intense TCs (wind speed > 64 knots) over the BoB experienced a longitudinal eastward shift of 2.3° during 1997–2014, compared to the period of 1981–1996. Another study found that the mean genesis location of TCs in the BoB moves to the east of 87°E during La Niña events and shifts to the west of 87°E during El Niño events (Girishkumar and Ravichandran 2012).

In summary, previous studies of BoB TC activity have mainly focused on interannual and decadal variability associated with ENSO and the PDO. Several studies also investigated the variability of TC genesis locations, with most focusing on the zonal movement in the BoB. Few studies paid attention to the meridional shift of TC activity, especially for the postmonsoon season. In the present study, we find a meridional oscillation in TC genesis locations in the postmonsoon BoB. During years when the average genesis location shifts northward (north-years) in the BoB,

the average landfall wind speed is more intense than that during years when the average genesis location displaces southward. These findings may have significant implications for the prediction of TCs as well as disaster prevention and mitigation over the BoB.

The rest of this paper is organized as follows. Section 2 introduces the data and the analysis method. Section 3 presents the results. Section 4 gives the conclusions and discussions.

2 Data and methodology

Tropical cyclones best track data for 1980–2015 is obtained from the Joint Typhoon Warning Center (JTWC). The data contains track positions and 6-hourly maximum sustained wind speed, which are used to calculate average genesis locations of TCs and accumulated cyclone energy (ACE). ACE is defined as the sum of the squares of 6-hourly maximum sustained wind speed. The TC categories are determined by the Saffir–Simpson Hurricane Wind Scale.

To analyze the influence of environmental factors on the genesis locations of TCs, monthly SST, sea level pressure, vertical and horizontal wind, air temperature, specific humidity, relative humidity and geopotential for the months of October–December during 1980–2015 are obtained from the European Center for Medium-Range Weather Forecasts' (ECWMF's) ERA-Interim reanalysis (Dee et al. 2011). We also use National Centers for Environmental Prediction/National Center for Atmospheric Research (NCEP/NCAR) reanalysis data (Kalnay et al. 1996) and Hadley SST data (Rayner et al. 2003) to verify the results based on the ERA-Interim reanalysis. Particularly, linear trends of all atmospheric and oceanic variables have been removed in the following analysis. Statistical significance is calculated using a two-tailed Student's *t* test.

Following Emanuel and Nolan (2004), we use the genesis potential index (GPI) to diagnose the influence of large-scale environmental factors on genesis locations. The GPI is defined as:

$$GPI = Term1 \times Term2 \times Term3 \times Term4, \quad (1)$$

where $Term1 = |10^5 \eta|^{3/2}$, $Term2 = (H/50)^3$, $Term3 = (1 + 0.1V_{shear})^{-2}$ and $Term4 = (V_{pot}/70)^3$. η is the absolute vorticity at 850 hPa, H is the relative humidity at 600 hPa, V_{shear} is the vertical wind shear between 200 and 850 hPa, and V_{pot} is the potential intensity (PI) defined by Bister and Emanuel (2002):

$$V_{pot}^2 = \frac{T_s}{T_o} \frac{C_k}{C_D} (CAPE^* - CAPE^b), \quad (2)$$

where T_s is the SST, T_o is the mean outflow temperature, C_k is the exchange coefficient for enthalpy, C_D is the drag coefficient. $CAPE^*$ is the convective available potential energy

(CAPE) of an air parcel lifted from saturation at sea level in reference to the environmental sounding, and $CAPE^b$ is the CAPE of ambient boundary layer air.

In order to investigate the relative contributions of each individual factor to the total GPI, we first take the natural logarithm at both sides of Eq. (1), then apply a total differential to both sides and integrate from the monthly climatology to a specific month (Li et al. 2013). We obtain the following equation:

$$\delta GPI = \alpha_1 \times \delta Term1 + \alpha_2 \times \delta Term2 + \alpha_3 \times \delta Term3 + \alpha_4 \times \delta Term4, \quad (3)$$

where $\alpha_1 = \frac{\overline{Term2} \times \overline{Term3} \times \overline{Term4}}{\overline{Term1} \times \overline{Term3} \times \overline{Term4}}$, $\alpha_2 = \frac{\overline{Term1} \times \overline{Term3}}{\overline{Term2} \times \overline{Term4}}$, $\alpha_3 = \frac{\overline{Term1} \times \overline{Term2} \times \overline{Term4}}{\overline{Term1} \times \overline{Term2} \times \overline{Term3}}$, $\alpha_4 = \frac{\overline{Term1} \times \overline{Term2} \times \overline{Term3}}{\overline{Term1} \times \overline{Term2} \times \overline{Term3}}$, a bar represents the monthly climatology,

$$\mathbf{W} = \frac{p \cos \varphi}{2000|\mathbf{U}|} \begin{pmatrix} \frac{U}{a^2 \cos^2 \varphi} \left[\left(\frac{\partial \psi'}{\partial \lambda} \right)^2 - \psi' \frac{\partial^2 \psi'}{\partial \lambda^2} \right] + \frac{V}{a^2 \cos \varphi} \left[\frac{\partial \psi'}{\partial \lambda} \frac{\partial \psi'}{\partial \varphi} - \psi' \frac{\partial^2 \psi'}{\partial \lambda \partial \varphi} \right] \\ \frac{U}{a^2 \cos \varphi} \left[\frac{\partial \psi'}{\partial \lambda} \frac{\partial \psi'}{\partial \varphi} - \psi' \frac{\partial^2 \psi'}{\partial \lambda \partial \varphi} \right] + \frac{V}{a^2} \left[\left(\frac{\partial \psi'}{\partial \varphi} \right)^2 - \psi' \frac{\partial^2 \psi'}{\partial \varphi^2} \right] \\ \frac{f_0^2}{N^2} \left\{ \frac{U}{a \cos \varphi} \left[\frac{\partial \psi'}{\partial \lambda} \frac{\partial \psi'}{\partial z} - \psi' \frac{\partial^2 \psi'}{\partial \lambda \partial z} \right] + \frac{V}{a} \left[\frac{\partial \psi'}{\partial \lambda} \frac{\partial \psi'}{\partial z} - \psi' \frac{\partial^2 \psi'}{\partial \varphi \partial z} \right] \right\} \end{pmatrix} \quad (7)$$

and δ denotes the difference between a specific month and the monthly climatology.

To understand the influences of specific humidity and air temperature on relative humidity, the relation between them is expressed as follows (Bolton 1980; Balaguru et al. 2016):

$$H \approx 0.263pq \left[\exp \left(\frac{17.67(T - T_{ref})}{T - 29.65} \right) \right]. \quad (4)$$

Here p is pressure (Pa), q is specific humidity (kg kg^{-1}), T is air temperature (K), and T_{ref} is 273.16 K. Using a similar method as for the GPI decomposition, the contributions of specific humidity and air temperature to relative humidity are computed. The moisture flux convergence is calculated as follows (Balaguru et al. 2016):

$$MFC = - \left[\nabla \cdot (qV_H) + \frac{\partial(q\omega)}{\partial p} \right], \quad (5)$$

where MFC is the moisture flux convergence, q is the specific humidity, p is the pressure, V_H is the horizontal velocity, and ω is the vertical velocity.

The zonal mass streamfunction ψ between 5°S and 5°N is used to diagnose the changes in Walker circulation. ψ is defined by Yu and Zwiers (2010) and Yu et al. (2012):

$$\psi = \frac{a\Delta\varphi}{g} \int_0^p u dp, \quad (6)$$

where a is the radius of Earth, g is the acceleration of gravity, $\Delta\varphi$ is the width between 5°S and 5°N in radians, u is the zonal wind and p is the pressure. In order to calculate the zonal mass streamfunction, first ψ in the boundary ($p = p_s$, $p = p_0$) is set to zero. Then, we calculate ψ_1 , with zonal wind integrated from the bottom ($p = p_s$) to the top ($p = p_0$), and ψ_2 , from the top to the bottom. Two linear weighting functions $\omega_1 = p/p_s$ and $\omega_2 = 1 - p/p_s$ are used to calculate the weighted mass streamfunction as $\psi = \omega_1\psi_1 + \omega_2\psi_2$. Finally, we obtain the zonal mass streamfunction ψ (Wang 1994; Gon et al. 2002).

Following Takaya and Nakamura (2001), the wave-activity flux \mathbf{W} is estimated to diagnose stationary Rossby wave propagation:

where p is pressure, λ is longitude, φ is latitude, f is the Coriolis parameter, a is the radius of Earth, $\mathbf{U} = (U, V)$ is the basic flow, N^2 is the buoyancy frequency squared, $\psi' = \Phi'/f$ is the perturbation geostrophic streamfunction, and Φ' is the geopotential anomaly. The wave-activity flux is independent of the wave phase and is parallel to the local group velocity of a stationary Rossby wave train. Hence, the wave-activity flux can describe a propagating packet of stationary or migratory quasi-geostrophic wave disturbances (Kosaka and Nakamura 2006; Shi et al. 2016).

3 Results

3.1 Meridional oscillation in genesis locations and its influences on TC activity

The time series of the average genesis latitude of TCs in the postmonsoon BoB during the satellite era of 1980–2015 is shown in Fig. 1a. It reveals that the average genesis location has an obvious meridional oscillation. To investigate the causes of the meridional oscillation of TC genesis location and its possible influence on TC activity, we define the years that the latitude of the average genesis location is greater (less) than the mean value plus (minus) half of the standard deviation as north-years (south-years), and these are shown as red (blue) circles in Fig. 1a. This classification gives five

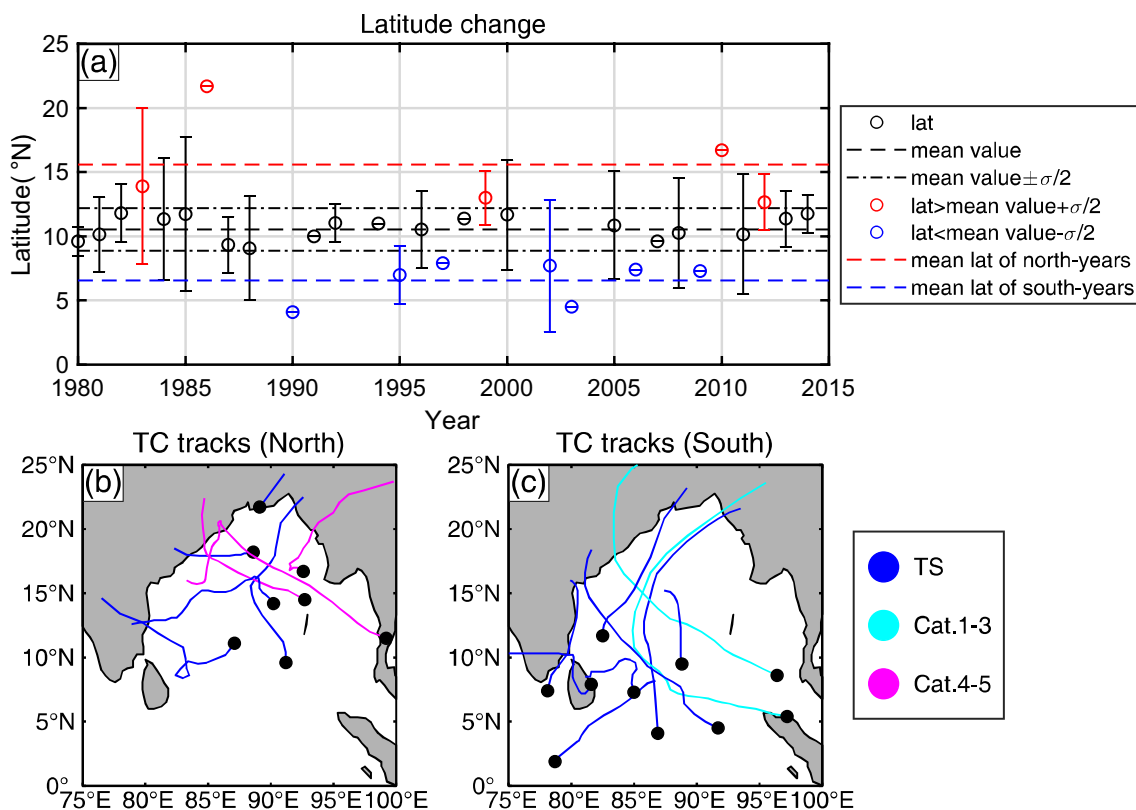


Fig. 1 a Time series of the average genesis latitude of TCs in the postmonsoon (October–December) BoB during 1980–2015. The error bar represents the standard deviation of latitudes in each year. b, c TC tracks in north-years and south-years of TC genesis locations.

In b and c, the black dots denote the genesis locations and the colored lines represent the TC tracks. The blue, cyan and magenta indicate tropical storm (TS), category 1–3 TC and category 4–5 TC, respectively

Table 1 TC number in north-years and south-years of TC genesis locations

| | North | South |
|----------|----------|-----------|
| Cat. 4–5 | 3 (0.60) | 0 (0.0) |
| Cat. 1–3 | 0 (0.00) | 2 (0.29) |
| TS | 5 (1.00) | 8 (1.14) |
| Total | 8 (1.60) | 10 (1.43) |

Values in parentheses indicate the annual means

north-years and seven south-years of TC genesis locations. During north-years, eight TCs formed in the BoB (1.6 TCs per year on average): three were category 4–5 and five were TS. During south-years of TC genesis locations, ten TCs formed in the BoB (1.4 TCs per year), out of which two were category 1–3 and eight were TS (Table 1). The annual mean number of TCs and number of intense TCs in north-years of TC genesis locations are both larger than in south-years. This may be a little counterintuitive since one would expect TCs that form in the south to have more time over the ocean before landfall and hence higher intensities. To understand more about TC activity during north-years and south-years

of TC genesis locations, ACE, a suitable TC energy metric, is examined.

Figure 2a shows that the average ACE for TCs in north-years is nearly twice as much as in south-years, indicating that more intense TC activity occurs in north-years. ACE is related to TC number, intensity and duration. The mean maximum wind speed is 40.2% greater in north-years than in south-years (Fig. 2b). However, the mean TC durations in the two periods are nearly the same (Fig. 2c). It clearly indicates that the difference in ACE can be attributed to differences in TC intensity. In addition, the mean wind speed at landfall is far more intense in north-years than in south-years. The difference between them is statistically significant at the 90% level (Fig. 2d). Hence, the impacts of TCs may be more severe over the coastal areas of India and Bangladesh in north-years.

3.2 Influence of environmental factors on genesis location

There are several environmental factors, including low-level relative vorticity, Coriolis parameter, SST, vertical wind shear, conditional instability through a deep atmospheric

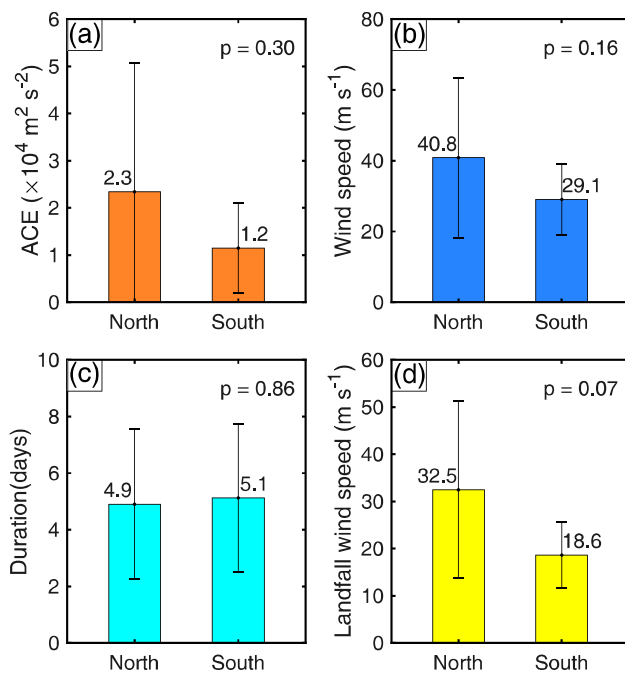


Fig. 2 Average of **a** ACE, **b** maximum sustained wind speed, **c** duration and **d** landfall maximum wind speed for each TC in north-years and south-years of TC genesis locations. The error bar represents the standard deviation. The p-value in each panel is based on a two-tailed Student's *t* test for difference of means between north-years and south-years

layer, and mid-troposphere relative humidity (Gray 1968), that play an important role in TC genesis. To understand the cause of the meridional oscillation of TC genesis locations, we use composite analysis to investigate the influence of environmental factors on genesis locations. Figure 3a, b show the composites of SST anomalies during north-years and south-years of TC genesis locations, respectively, calculated as the monthly SST anomalies averaged over the five north-years and seven south-years of TC genesis locations for the months of October–December. The difference between the SST anomalies in north-years and south-years of TC genesis locations is shown in Fig. 3c. The difference is defined as the composite for north-years of TC genesis locations minus that of south-years of TC genesis locations. There are negative SST anomalies covering almost the entire basin for north-years of TC genesis locations relative to south-years (Fig. 3a). However, the negative SST anomalies are much stronger in the southern BoB than in the northern BoB, which tends to favor a northward shift of TC genesis locations. In south-years of TC genesis locations, positive SST anomalies are found over the central and southern part of the BoB (Fig. 3b). The positive SST anomalies are more favorable for the genesis of TCs in south-years of TC genesis locations.

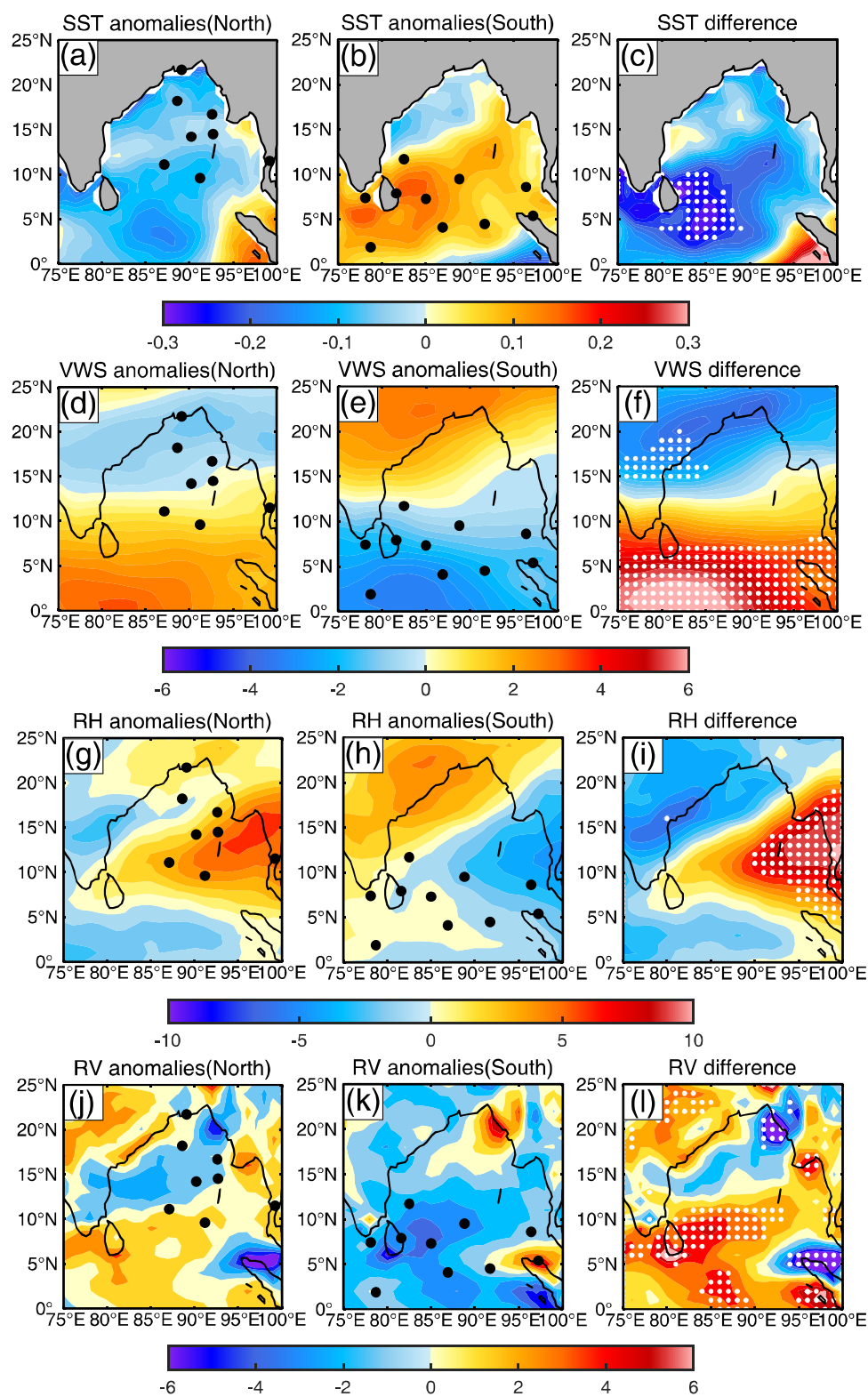
To the north of 13°N vertical wind shear is weaker during north-years, while stronger vertical wind shear exists to the south of 13°N (Fig. 3d). The opposite pattern happens in south-years of TC genesis locations (Fig. 3e). Indeed, the structure of vertical wind shear anomalies is consistent with variability of the cyclone genesis locations during the two periods. Namely, when negative vertical wind shear anomalies appear in the northern (southern) BoB, the TC genesis locations shift northward (southward). TCs also tend to form in the region of positive relative humidity anomalies over the northeastern (southwestern) BoB in north-years (south-years) of TC genesis locations (Fig. 3g, h). The positive anomalies of relative vorticity are mostly in the southern part of the BoB in north-years (Fig. 3j), and there are negative anomalies in most of the basin in south-years of TC genesis locations (Fig. 3k). The pattern of relative vorticity anomalies indicates that it is not the key parameter that controls the variability of genesis locations in the BoB.

3.3 GPI analysis

To further understand the influence of environmental parameters, we calculate the GPI and the contributions from each factor. Figure 4c, d show the GPI anomalies in north-years and south-years of TC genesis locations, respectively. In Fig. 4f, g, the linear sums of contributions of each term to GPI in the two periods are consistent with the original GPI. Several studies have also shown that the contributions of the nonlinear terms to GPI are weak (e.g., Camargo et al. 2009; Jiang et al. 2012; Li et al. 2013; Balaguru et al. 2016; Wang et al. 2017). It is thus reasonable to estimate the contributions of each term to GPI using the linear method based on Eq. (3). There are positive GPI anomalies in the northeastern BoB during north-years of TC genesis locations, while positive GPI anomalies exist in the southwestern BoB during south-years of TC genesis locations. This is consistent with the variability of TC genesis locations during the two periods.

Figure 5 shows the contributions of each term to GPI, including absolute vorticity, relative humidity, vertical wind shear and potential intensity. In north-years, the TC genesis locations tend to be in the regions where there are positive GPI anomalies from low-level vorticity and relative humidity (Fig. 5a, d). The relative humidity dominates the positive contributions of GPI. In contrast, in south-years, the TC genesis locations tend to situate in the regions where there are positive GPI anomalies from vertical wind shear, relative humidity and potential intensity (Fig. 5e, h, k). The positive GPI contributions from the vertical wind shear term are dominant, while the positive GPI contributions from relative humidity and potential intensity term are relatively small, especially for potential intensity. Above all, the vertical wind shear and relative humidity are the primary factors driving

Fig. 3 Composites of **a, b** SST ($^{\circ}\text{C}$) anomalies, **d, e** vertical wind shear (m s^{-1}) anomalies, **g, h** 600 hPa relative humidity (%) anomalies, and **j, k** 850 hPa relative vorticity (10^{-6} s^{-1}) anomalies for north-years and south-years of TC genesis locations, averaged over October–December. The black dots denote the genesis locations during north-years and south-years of TC genesis locations. Also shown is the composite differences of **c** SST ($^{\circ}\text{C}$), **f** vertical wind shear (m s^{-1}), **i** 600 hPa relative humidity (%) and **l** 850 hPa relative vorticity (10^{-6} s^{-1}). The composite difference is defined as the composite for north-years minus that of south-years of TC genesis locations. The white dots denote values that are statistically significant at the 90% level

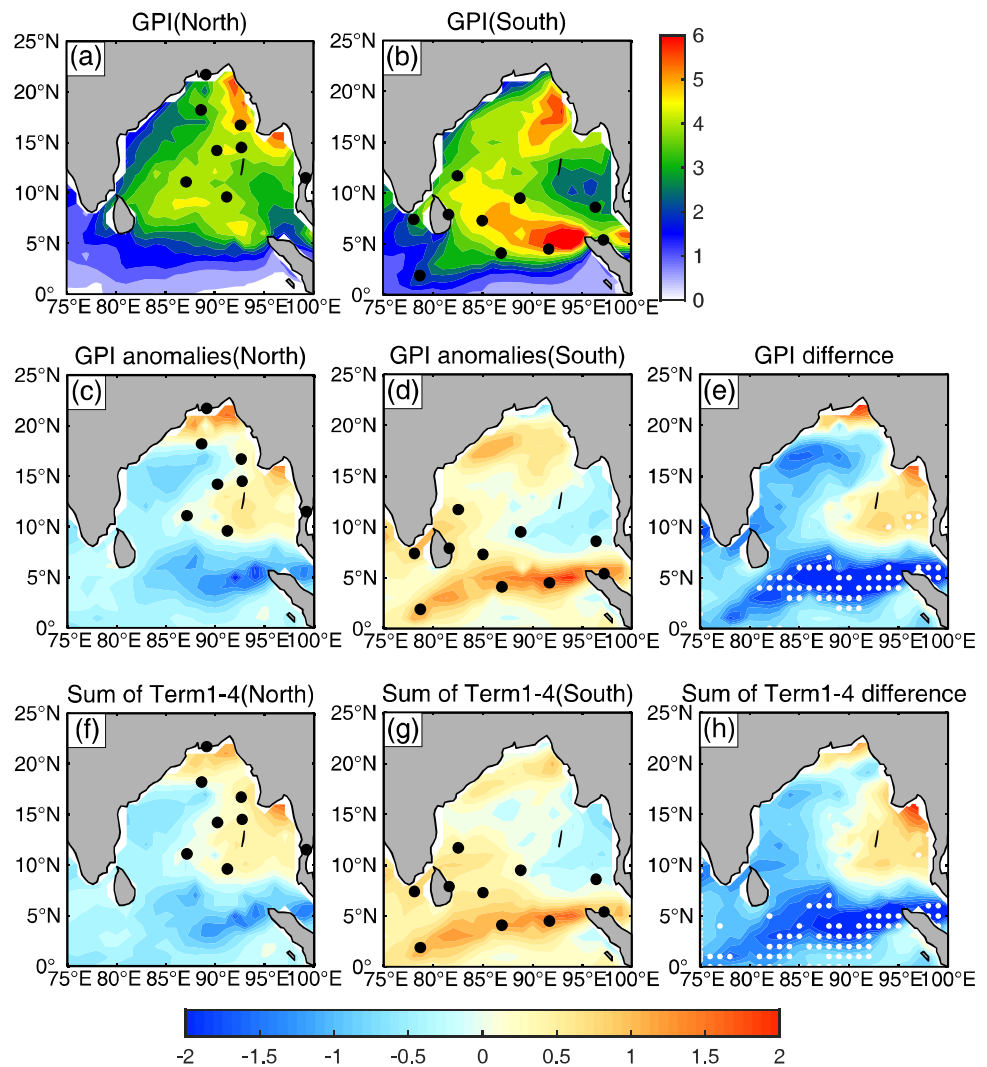


the meridional oscillation of TC genesis locations, which is consistent with the results in Sect. 3.2.

To understand the changes in atmospheric environmental factors, we examine the changes in the atmospheric

circulation. In north-years of TC genesis locations, there are anomalous westerlies at low levels in the southern (northern) BoB (Fig. 6e), indicating enhancement (reduction) of the mean westerlies (easterlies). At upper levels,

Fig. 4 Composites of **a, b** GPI, **c, d** GPI anomalies, and **f, g** sum of contributions of each term for north-years and south-years of TC genesis locations. The black dots denote the genesis locations during north-years and south-years of TC genesis locations. Composite differences of **e** GPI and **h** sum of contributions of each term between north-years and south-years of TC genesis locations. The white dots denote values that are statistically significant at the 90% level. The composites shown are averaged over October–December



the easterlies (westerlies) become stronger (weaker) over the southern (northern) BoB in north-years of TC genesis locations (Fig. 6g). Together, these changes in upper- and lower-level circulation increase (decrease) the vertical wind shear in the southern (northern) BoB in north-years of TC genesis locations. The opposite is generally true in south-years (Fig. 6f, h).

To investigate the changes in relative humidity, we examine the separate contributions from specific humidity and air temperature according to Eq. (4). Figure 7 shows that the patterns of the specific humidity term are similar to the distributions of relative humidity, indicating that relative humidity is dominated by specific humidity. There is enhanced moisture flux convergence in the northeastern BoB in north-years of TC genesis locations (Fig. 8). In contrast, enhanced moisture flux convergence appears in the southwestern BoB in south-years of TC genesis locations. The distributions of moisture flux convergence anomalies are consistent with those of horizontal wind and relative

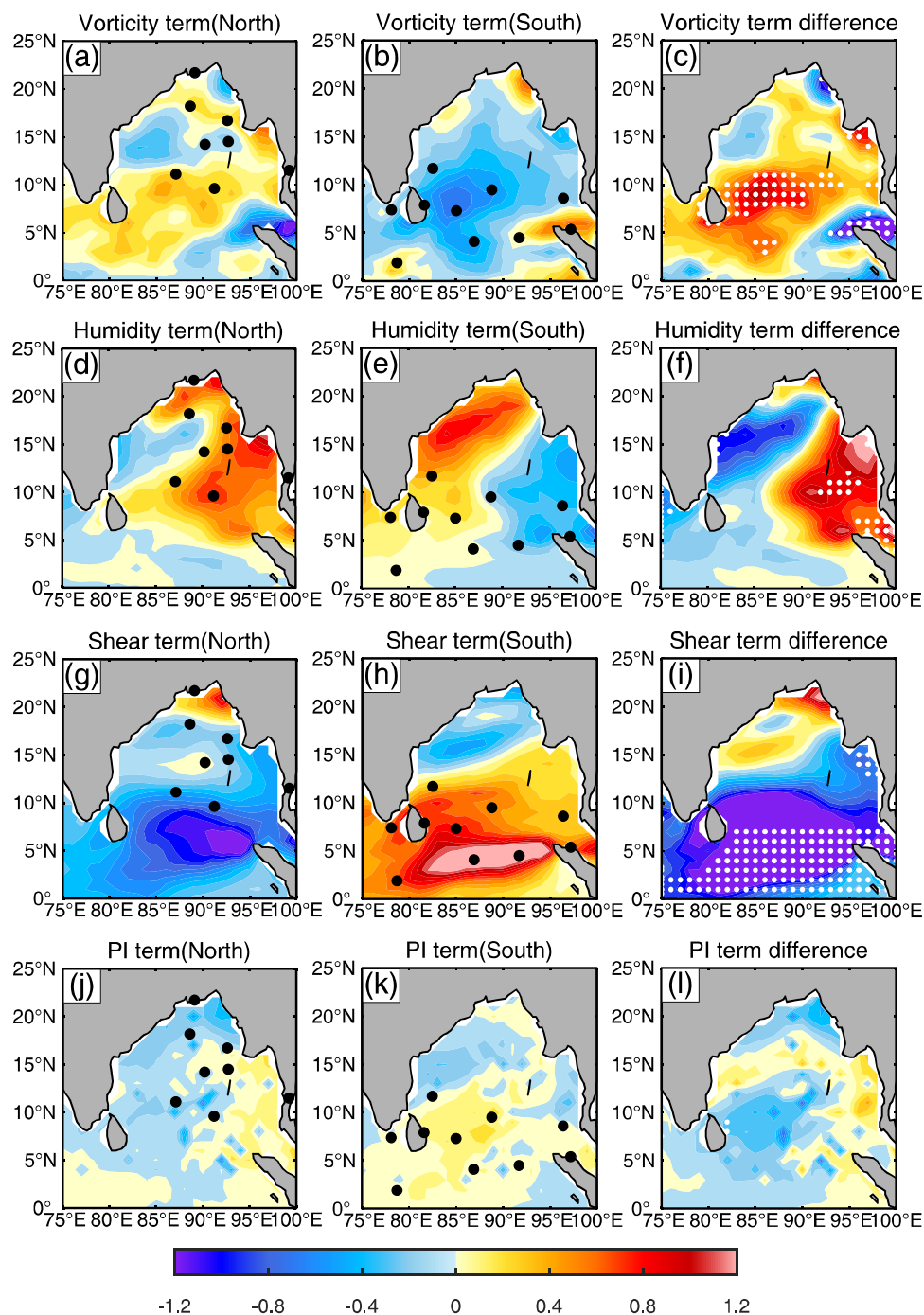
humidity anomalies (Figs. 5, 6), suggesting that the atmospheric circulation significantly affects the variability of relative humidity.

3.4 Remote influence of ENSO and PDO

Next, we attempt to understand what causes the changes in atmospheric circulation. Figure 9 shows the global composite SST anomalies in north-years and south-years of TC genesis locations. The SST anomalies show a La Niña-like pattern (El Niño-like pattern) in the equatorial Pacific for north-years (south-years) of TC genesis locations. It indicates that ENSO and the PDO may exert an influence on the meridional oscillation of TC genesis location.

To understand atmospheric circulation variability in the tropical Indian Ocean, we examine the zonal mass streamfunction between 5°S and 5°N. The Indian Ocean branch of the Walker circulation strengthens (weakens) during north-years (south-years) of TC genesis locations (Fig. 10).

Fig. 5 Same as in Fig. 3, but for contributions of 850 hPa absolute vorticity, 600 hPa relative humidity, vertical wind shear and potential intensity to GPI



This strengthening is consistent with what is expected during La Niña events. Furthermore, the velocity potential and divergent wind show anomalous convergence (divergence) at low levels (upper levels) over Indonesia and anomalous divergence (convergence) at low levels (upper levels) over the western tropical Indian Ocean in north-years of TC genesis locations. The opposite pattern exists in south-years of TC genesis locations (Fig. 11). Accordingly, there are clear anomalous westerlies (easterlies) at low levels in the tropical Indian Ocean in north-years (south-years) (Fig. 6e, f).

At upper levels, there are anomalous easterlies (westerlies) in the tropical Indian Ocean in north-years (south-years) of TC genesis locations (Fig. 6g, h). The convergence (divergence) of moisture over the northeastern BoB in north-years (south-years) also corresponds to the divergent wind shown in Fig. 11. In north-years (south-years) of TC genesis locations, the anomalous updraft (downdraft) above the Indonesia transports more (less) moisture into the mid-troposphere, increasing (reducing) the relative humidity over the northeastern BoB, which is close to Indonesia. Hence, the

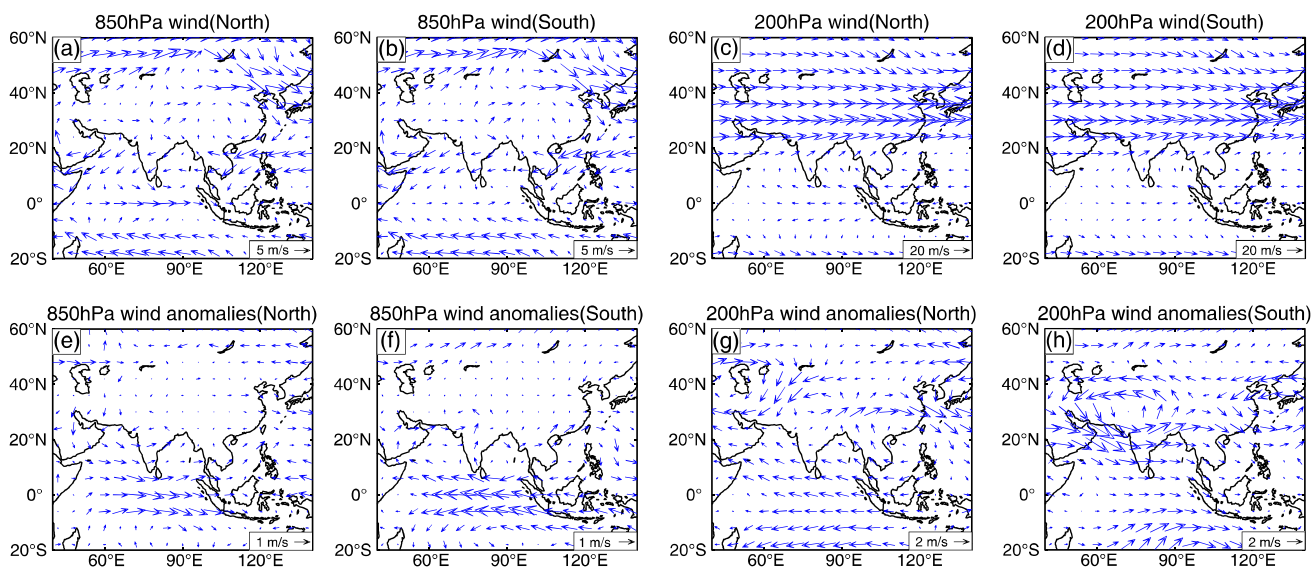
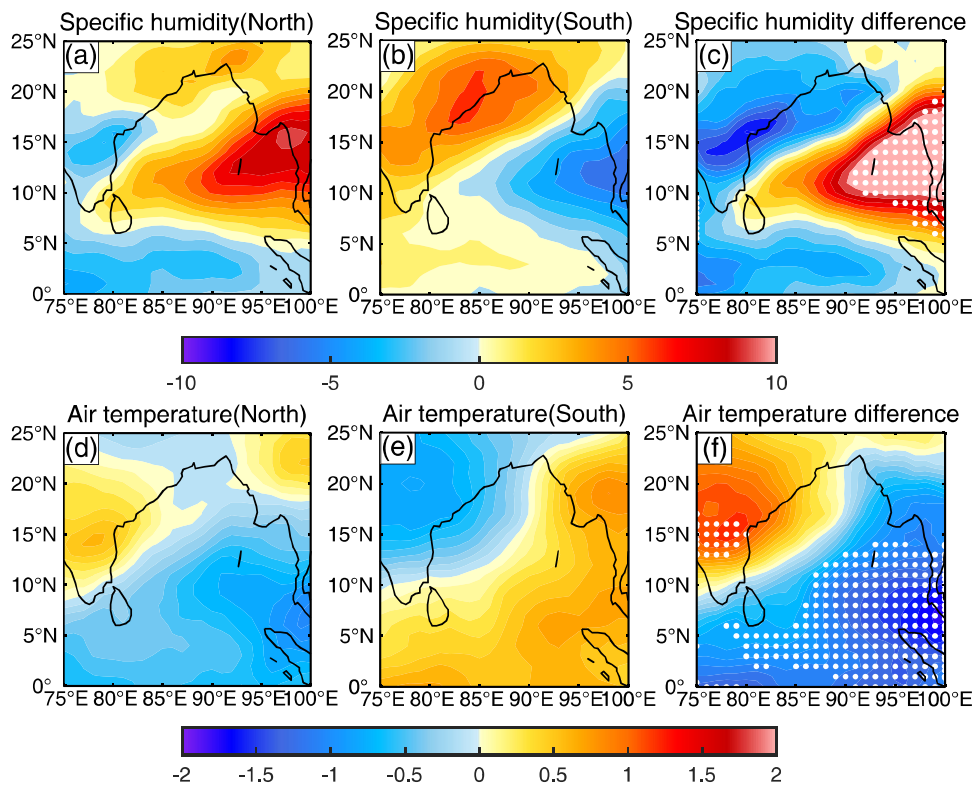


Fig. 6 Composites of horizontal wind at **a, b** 850 hPa and **c, d** 200 hPa for north-years and south-years of TC genesis locations, respectively. Composites of horizontal wind anomalies at **e, f** 850 hPa

and **g, h** 200 hPa, for north-years and south-years of TC genesis locations, respectively. The composites shown are averaged over October–December

Fig. 7 Composites of the contributions of **a, b** specific humidity and **d, e** air temperature to relative humidity for north-years and south-years of TC genesis locations, averaged over October–December, respectively. Composite differences of **c** specific humidity and **f** air temperature’s contributions between north-years and south-years of TC genesis locations. The white dots denote values that are statistically significant at the 90% level

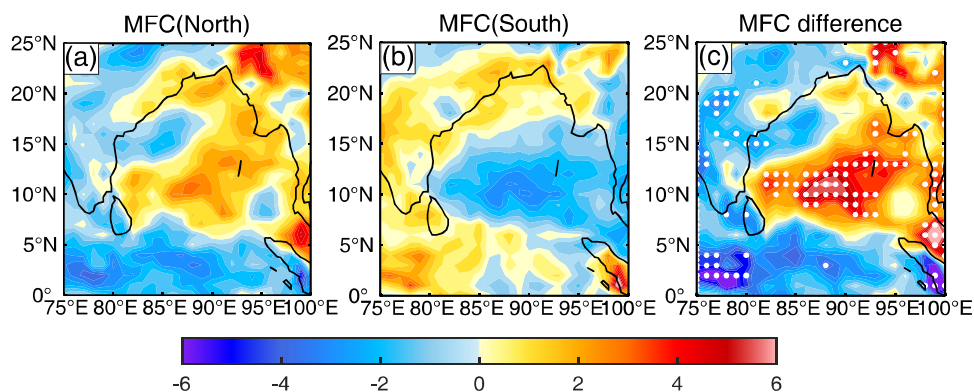


above analysis shows that changes in the Walker circulation may explain the variation of vertical wind shear and relative humidity over the tropical Indian Ocean.

One can also see that there is a downdraft (an updraft) anomaly above the Iranian Plateau (east of Iranian Plateau) in north-years (south-years) of TC genesis locations

(Fig. 11). It is consistent with an anticyclonic (cyclonic) anomaly at upper levels over the Iranian Plateau (east of Iranian Plateau) in north-years (south-years) (Fig. 6g, h). Further, the wave-activity flux is examined to understand the changes in atmospheric circulation over the extratropical region (Fig. 12). In the calculation, the climatological

Fig. 8 Composites of **a, b** moisture flux convergence ($10^{-9} \text{ kg kg}^{-1} \text{ s}^{-1}$) anomalies for north-years and south-years of TC genesis locations, averaged over October–December, respectively. Composite difference of **c** moisture flux convergence ($10^{-9} \text{ kg kg}^{-1} \text{ s}^{-1}$) between north-years and south-years of TC genesis locations. The white dots denote values that are statistically significant at the 90% level



geostrophic wind from 1980 to 2015 for the months of October–December is taken as the background flow. The geopotential anomalies for the north-years and the south-years are used to calculate the perturbation geostrophic streamfunction, respectively. It is seen that there is a stationary Rossby wave train propagating from the North Pacific to the Iranian Plateau (east of Iranian Plateau), generating positive (negative) geopotential height anomalies in north-years

(south-years) of TC genesis locations due to the changes of SST in the equatorial Pacific (Fig. 12). Hence, the stationary Rossby wave train may distinctly influence the extratropical atmospheric circulation. The patterns of geopotential height anomalies induced by the stationary Rossby wave train are consistent with those of upper-level wind anomalies in north-years and south-years (Fig. 6g, h). It can be seen from Fig. 6e, f that the difference in low-level wind anomalies between north-years and south-years is negligibly small over the extratropical Indian Ocean. However, there are weak (strong) easterly (westerly) anomalies near 20°N in the upper troposphere in north-years (south-years) of TC genesis locations. These therefore reduce (increase) the vertical wind shear in the northern BoB in north-years (south-years) of TC genesis locations. In summary, due to the phase shift of SST anomalies in the equatorial Pacific, the tropical Walker circulation in conjunction with the extratropical stationary Rossby wave train induce atmospheric circulation variability over the entire NIO, which in turn results in the opposite patterns of vertical wind shear and relative humidity for north-years and south-years of TC genesis locations.

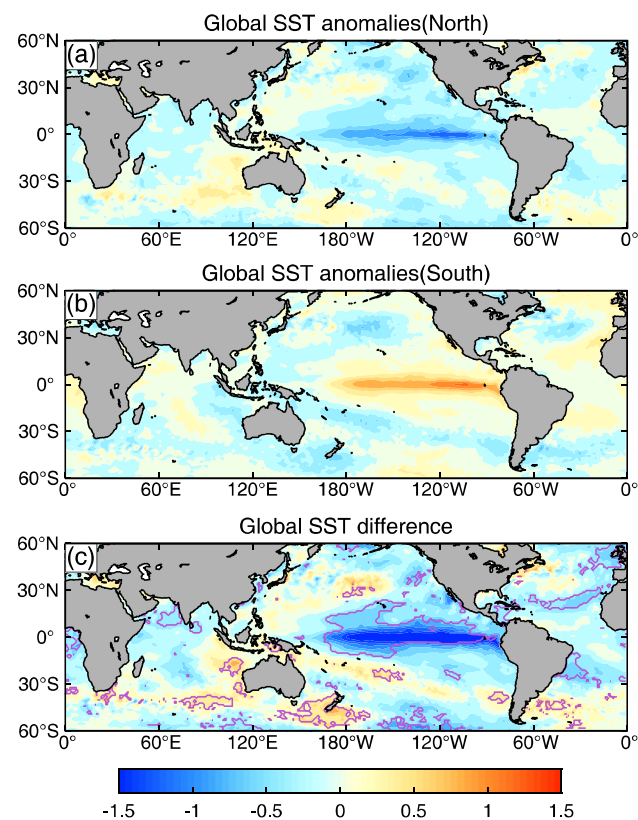


Fig. 9 Composites of **a, b** global SST ($^{\circ}\text{C}$) anomalies for north-years and south-years of TC genesis locations, averaged over October–December, respectively. Composite difference of **c** global SST ($^{\circ}\text{C}$) between north-years and south-years of TC genesis locations. The purple contour denotes values that are statistically significant at the 90% level

To further understand the influence of ENSO and the PDO on the TC genesis locations, we calculate the correlation coefficient between normalized time series of the average genesis latitude of TCs and averaged Niño3.4 index for October–December. The correlation coefficient is -0.19, with the significance below the 90% level. This is distinct from the composite analysis presented in Fig. 9, which shows significant differences in equatorial Pacific SST for north-years relative to south-years when years with weak anomalies (less than 0.5 standard deviations from the mean) are excluded. The 15-year moving correlation coefficient for all years is shown in Fig. 13a. By considering all years, we can examine temporal changes in the Pacific influence on the BoB. Before 1997, the correlation coefficient between the normalized time series of the average genesis latitudes of TCs and Niño3.4 index is low, with less significance. However, since 1998, the negative correlation is strong, with significance beyond the 90% level.

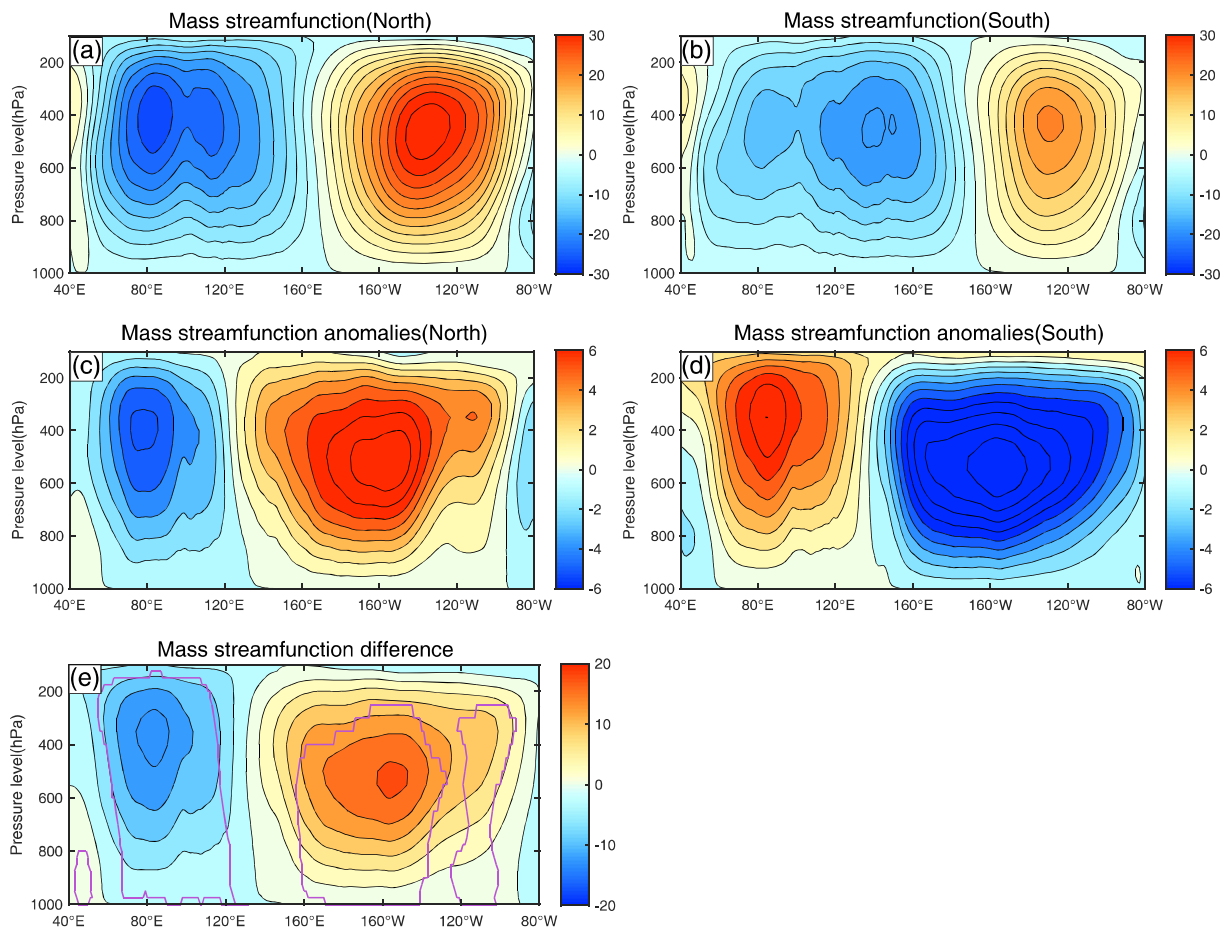


Fig. 10 Composites of **a, b** mass streamfunction (10^9 kg s^{-1} , contour interval: $3 \times 10^9 \text{ kg s}^{-1}$) between 5°S and 5°N for north-years and south-years of TC genesis locations, respectively. Composites of **c, d** mass streamfunction (10^9 kg s^{-1} , contour interval: $1 \times 10^9 \text{ kg s}^{-1}$) anomalies between 5°S and 5°N for north-years and south-years of

TC genesis locations, respectively. Composite difference of **e** mass streamfunction (10^9 kg s^{-1} , contour interval: $3 \times 10^9 \text{ kg s}^{-1}$) between north-years and south-years of TC genesis locations. The composites shown are averaged over October–December. The purple contour denotes values that are statistically significant at the 90% level

To investigate why the relationship changes between the time series of the average genesis latitudes of TCs and the Niño 3.4 index, we divide the 36 years into two periods according to the regime shift of the PDO. The first epoch is from 1980 to 1997 (epoch-I) and the second is from 1998 to 2015 (epoch-II) (e.g., Wang and Liu 2015; Wang et al. 2015; Zhao et al. 2018). In epoch-I, the correlation between the GPI and the Niño 3.4 index is positive in the western and southern BoB and negative in the eastern and northern BoB (Fig. 13b). During epoch-II, the pattern of the correlation is almost the same as in epoch-I, but the significance level is higher (Fig. 13c). It is consistent with the changes in correlation coefficient between the latitude time series and the Niño 3.4 index and indicates that the influence of ENSO has strengthened in epoch-II.

The changes in the relationship between TC genesis locations and ENSO may be related to the transition of the PDO phases. Previous studies showed that the warm phase of the

PDO persisted from 1977 to 1997, and the cold phase persisted from 1998 to 2015 (e.g., Wang and Liu 2015; Wang et al. 2015; Zhao et al. 2018). In epoch-I, during the warm phase of the PDO, the influence of ENSO on TC genesis is weak. However, the link between ENSO and TC genesis strengthens in epoch-II, corresponding to the cold phase of the PDO (Fig. 13). This indicates that the PDO can potentially modulate the influence of ENSO on the meridional oscillation of TC genesis locations. Figure 14 shows that the relationship between ENSO and the Walker circulation has weakened slightly in the Indian Ocean, while the link between ENSO and the extratropical region of the NIO strengthened in epoch-II, corresponding to the cold PDO phase. Hence, changes in the relationship between the TC genesis locations and ENSO may be mainly induced by the variability of the stationary Rossby wave train that originates from the equatorial Pacific in the different PDO phases.

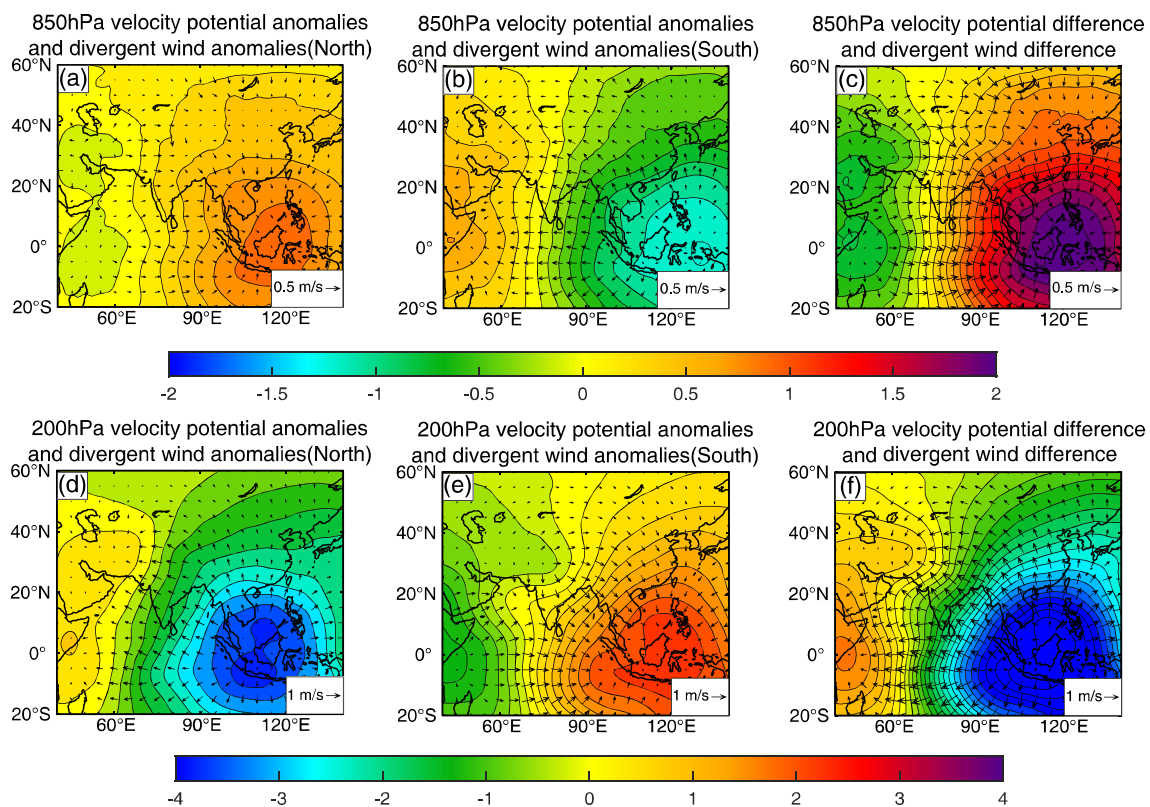


Fig. 11 Composites of **a, b** velocity potential anomalies ($10^6 \text{ m}^2 \text{ s}^{-1}$, contour interval: $0.15 \times 10^6 \text{ m}^2 \text{ s}^{-1}$) and divergent wind anomalies at 850 hPa for north-years and south-years of TC genesis locations, respectively. Composites of **d, e** velocity potential anomalies ($10^6 \text{ m}^2 \text{ s}^{-1}$, contour interval: $0.25 \times 10^6 \text{ m}^2 \text{ s}^{-1}$) and divergent wind

anomalies at 200 hPa for north-years and south-years of TC genesis locations, respectively. Composite differences of velocity potential ($10^6 \text{ m}^2 \text{ s}^{-1}$) and divergent wind at **c** 850 hPa and **f** 200 hPa between north-years and south-years of TC genesis locations. The composites shown are averaged over October–December

Indeed, several studies have found that the PDO can modulate the frequency and strength of ENSO phases, resulting in different thermodynamic and dynamic conditions in the ocean and atmosphere (e.g., Wu and Wang 2002; Kurtzman and Scanlon 2007; Yu and Zwiers 2007; Wang et al. 2008; Krishnamurthy and Krishnamurthy 2013). Global TC activity is also associated with modes of large-scale ocean–atmosphere climate variability (Mauw 2011). In the western North Pacific (WNP), an interdecadal variation of TC activity exists (e.g., Liu and Chan 2013; Yang et al. 2017). Zhao and Wang (2015) found that the PDO modulates ENSO and TC activity in the WNP during October–December, causing an enhancement of the ENSO–TC relationship in the cold PDO phase and a reduction in the warm phase. Rapid intensification of WNP TCs has been found to be influenced by both ENSO and the PDO (Wang and Liu 2015). A northwestward shift of TC genesis locations during boreal autumn in the WNP was observed and was attributed to the variability of ENSO (Hu et al. 2017). For the NIO region, Girishkumar et al. (2014b) suggested a modulation of the ENSO–TC relationship in the postmonsoon BoB by

the PDO, finding significant differences in ENSO’s effect on the extratropical region of the NIO during the different PDO phases. The results of our study are consistent with the findings from Girishkumar et al. (2014b). Compared to the studies in the WNP, our study highlights the combined effect of the Walker circulation and stationary Rossby wave train originating from ENSO and the possible modulation by the PDO through the midlatitude wave train. However, interactions between the PDO and ENSO are complicated and require comprehensive air–sea coupled model studies for in-depth insight.

4 Conclusions and discussions

In this study, the average genesis locations of TCs in the postmonsoon BoB are investigated during 1980–2015. The results reveal that there is a distinct meridional oscillation in the average genesis locations of TCs. In north-years of TC genesis locations, the number of TCs attaining category 4–5 intensity is more than in south-years. Both average intensity

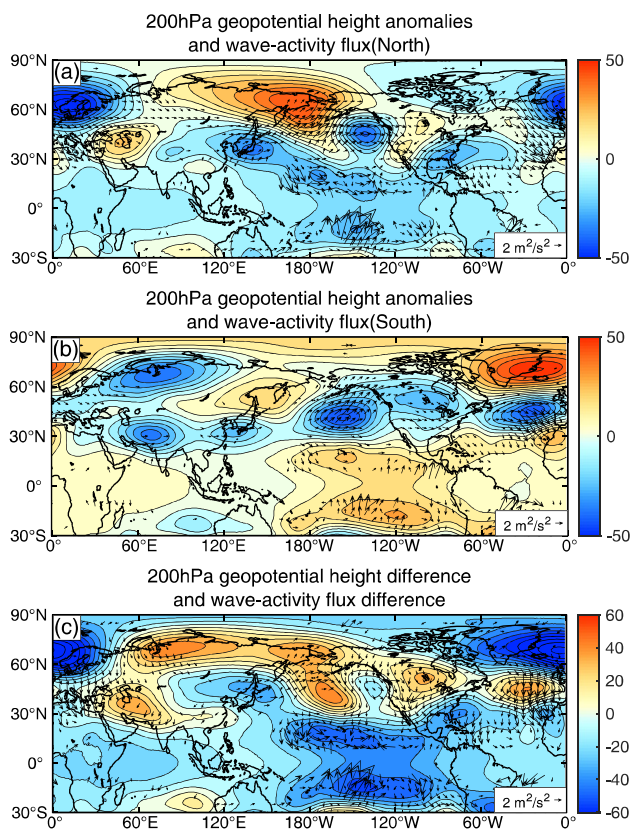


Fig. 12 Composites of **a**, **b** geopotential height (gpm, contour interval: 6 gpm) anomalies and wave-activity flux (only show the magnitude exceeds $1 m^2 s^{-2}$) at 200 hPa for north-years and south-years of TC genesis locations, respectively. Composite differences of **c** geopotential height (gpm, contour interval: 8 gpm) and wave-activity flux (only show the magnitude exceeds $1 m^2 s^{-2}$) at 200 hPa between north-years and south-years of TC genesis locations. The composites shown are averaged over October–December

and landfall intensity in north-years of TC genesis locations are more intense than in south-years. Analysis of ERA-Interim shows that weak vertical wind shear and enhanced relative humidity over the northern BoB is favorable for TC formation in north-years of TC genesis locations, while TCs tend to form over the southern BoB in south-years of TC genesis locations because of warm SST, weak vertical wind shear and high relative humidity. The patterns of GPI anomalies are consistent with the TC genesis locations during the two periods. Furthermore, in north-years of TC genesis locations, the contributions of each factor to GPI show that relative humidity induces the distinctly positive anomalies of GPI over the northern BoB, while the vertical wind shear causes strongly negative anomalies of GPI over the southern BoB. These environmental conditions are more favorable for TCs to form over the northern BoB during north-years of TC genesis locations. In contrast, there are positive contributions from vertical wind shear over the southern BoB in south-years of TC genesis locations. The relative humidity

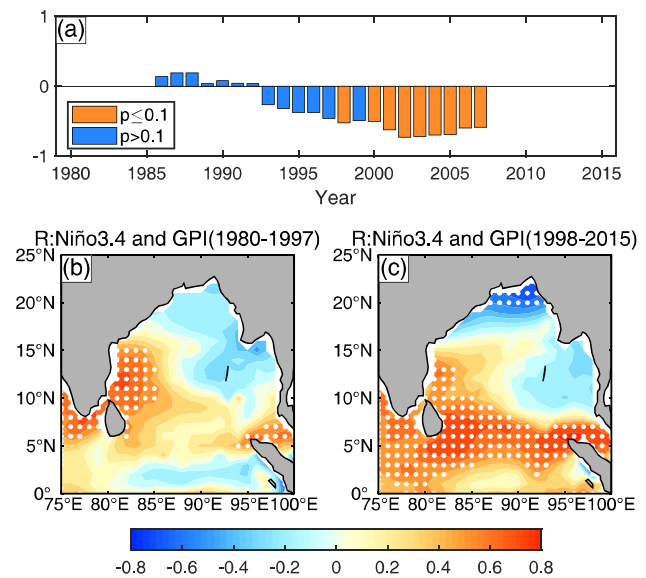


Fig. 13 **a** 15-year moving correlation coefficient between the normalized latitude time series and Niño 3.4 index. The horizontal axis represents the middle year of each 15-year period. **b**, **c** Correlation between GPI and Niño 3.4 index, for the period of 1980–1997 and 1998–2015. The Niño 3.4 index is averaged over October–December. The white dots denote values that are statistically significant at the 95% level

and SST also make positive contributions in the southern BoB, with relatively small magnitudes, compared to the vertical wind shear. A similar analysis performed by using NCEP/NCAR reanalysis confirms the results (not shown).

Further analysis reveals that changes in the vertical wind shear and relative humidity can be attributed to the changes in atmospheric circulation over the BoB. We find that the SST anomalies over the equatorial Pacific show a La Niña-like (El Niño-like) pattern during north-years (south-years) of TC genesis locations. Due to the changes of SST in the equatorial Pacific, in north-years (south-years) of TC genesis locations, the enhanced (weakened) Walker circulation strengthens (reduces) the westerlies at low levels and strengthens (reduces) the easterlies at upper levels over the tropical Indian Ocean. These increase (decrease) the vertical wind shear over the southern BoB and increase (decrease) relative humidity over the northern BoB during north-years (south-years) of TC genesis locations. In addition, a stationary Rossby wave train propagates from the North Pacific to the Iranian Plateau (east of Iranian Plateau), generating positive (negative) geopotential height anomalies that induces an anomalous downdraft (updraft) in north-years (south-years) of TC genesis locations over the extratropical region of NIO. This weakens (strengthens) the westerlies at upper levels over the northern BoB. Hence, the vertical wind shear decreases (increases) over the northern BoB in north-years (south-years) of TC genesis locations. The combination of

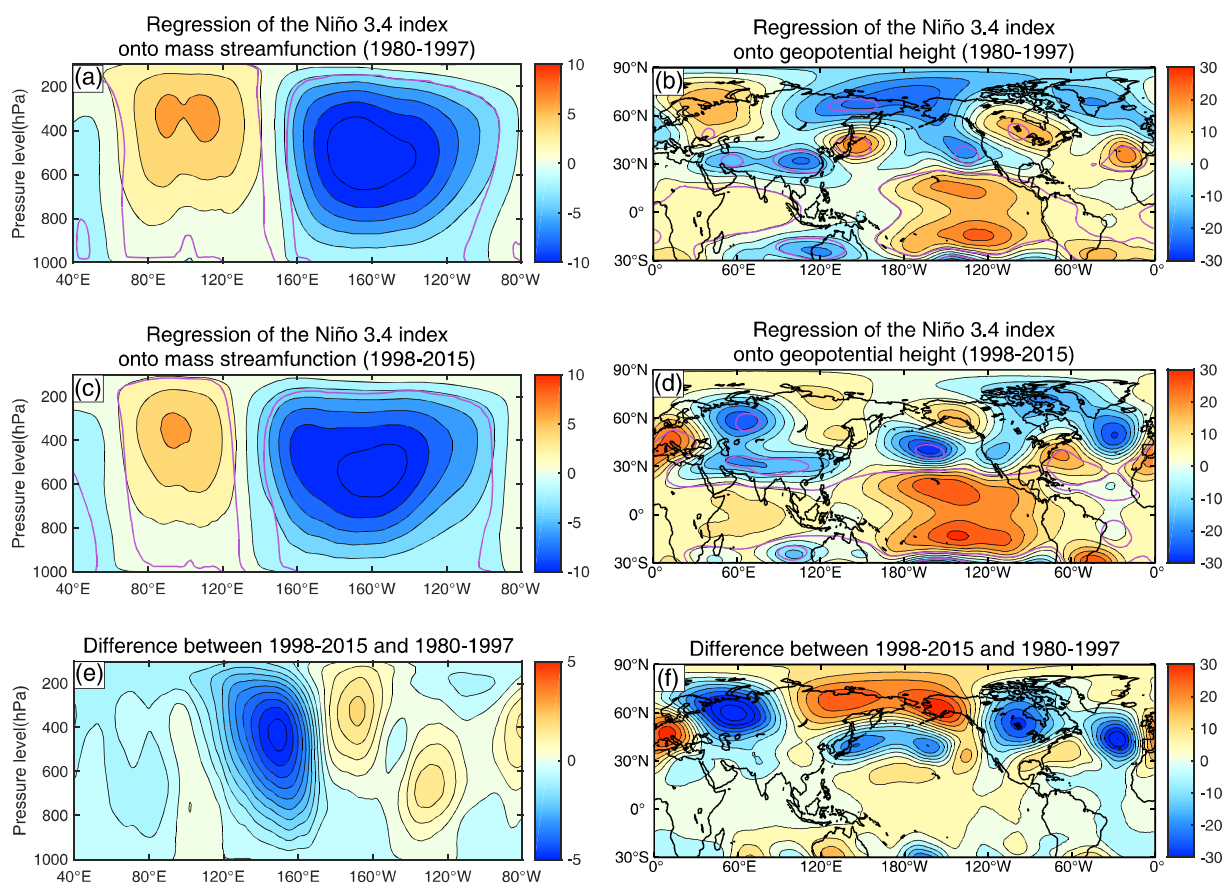


Fig. 14 **a, c** Regressions of the Niño 3.4 index onto mass streamfunction (10^9), for the period of 1980–1997 and 1998–2015, respectively. **b, d** Regressions of the Niño 3.4 index onto geopotential height, for the period of 1980–1997 and 1998–2015, respectively. Differences of regression coefficient between **e** mass streamfunction (10^9), **f** geo-

potential height and Niño 3.4 index between the period of 1998–2015 and 1980–1997. The Niño 3.4 index is averaged over October–December. Purple contour denotes values that are statistically significant at the 95% level

Walker circulation and stationary Rossby wave train tend to make the environmental conditions more conducive to TC formation over the northern (southern) BoB in north-years (south-years) of TC genesis locations. This therefore causes a meridional oscillation of the average TC genesis locations in postmonsoon BoB.

In addition, we find that the relationship between ENSO and the genesis locations is weak under the warm phase of the PDO, while it is strong under the cold phase of the PDO. A study also found that there is a difference in the relationship between ENSO and TC activity over the BoB under different phases of the PDO (Girishkumar et al. 2014b). It may be related to the different responses in atmospheric circulation induced by ENSO under different phases of the PDO. In this study, we highlight the importance of atmospheric teleconnections from ENSO and the PDO. However, there may be other local factors over the Indian Ocean that influence TC activity. For example, in north-years and south-years of TC genesis locations, SST anomalies show a weak IOD-like

pattern over the Indian Ocean. Hence, the atmospheric circulation may be also influenced by the IOD. Girishkumar et al. (2014a) also suggested that the patterns of GPI are different during different phases of the MJO. Hence, local variability of the atmosphere and ocean over the Indian Ocean may influence TC activity in the BoB. This is an important topic for future study.

Acknowledgements This study is supported by the National Natural Science Foundation (41776004), the Fundamental Research Funds for the Central Universities (2016B12514), the Opening Project of Key Laboratory of Marine Environmental Information Technology and the China Ocean Mineral Resources Research and Development Association Program (DY135-E2-3-02). GF was supported by base funds to NOAA/AOML. The authors sincerely acknowledge the use of TC best track data from Joint Typhoon Warning Center, and atmospheric and oceanic reanalysis from NCEP and ECMWF. Potential intensity is calculated using the MATLAB code available at [ftp://texmex.mit.edu/pub/manuel/TCMAX/](http://texmex.mit.edu/pub/manuel/TCMAX/). The Fortran code for calculating wave-activity flux can be downloaded from the website at <http://www.atmos.rcast.u-tokyo.ac.jp/nishii/programs/index.html>.

References

- Alam M, Hossain M, Shafee S (2003) Frequency of Bay of Bengal cyclonic storms and depressions crossing different coastal zones. *Int J Climatol* 23:1119–1125. <https://doi.org/10.1002/joc.927>
- Balaguru K, Taraphdar S, Leung L, Foltz G (2014) Increase in the intensity of postmonsoon Bay of Bengal tropical cyclones. *Geophys Res Lett* 41:3594–3601. <https://doi.org/10.1002/2014gl060197>
- Balaguru K, Leung L, Lu J, Foltz G (2016) A meridional dipole in premonsoon Bay of Bengal tropical cyclone activity induced by ENSO. *J Geophys Res Atmos* 121:6954–6968. <https://doi.org/10.1002/2016jd024936>
- Balaji M, Chakraborty A, Mandal M (2018) Changes in tropical cyclone activity in north Indian Ocean during satellite era (1981–2014). *Int J Climatol* 38:2819–2837. <https://doi.org/10.1002/joc.5463>
- Bister M, Emanuel K (2002) Low frequency variability of tropical cyclone potential intensity I. Interannual to interdecadal variability. *J Geophys Res* 107:4801. <https://doi.org/10.1029/2001jd000776>
- Bolton D (1980) The computation of equivalent potential temperature. *Mon Weather Rev* 108:1046–1053. [https://doi.org/10.1175/1520-0493\(1980\)108%3c1046:TCOEPT%3e2.0.CO;2](https://doi.org/10.1175/1520-0493(1980)108%3c1046:TCOEPT%3e2.0.CO;2)
- Camargo S, Wheeler M, Sobel A (2009) Diagnosis of the MJO modulation of tropical cyclogenesis using an empirical index. *J Atmos Sci* 66:3061–3074. <https://doi.org/10.1175/2009jas3101.1>
- Dee D et al (2011) The ERA-Interim reanalysis: configuration and performance of the data assimilation system. *Q J R Meteorol Soc* 137:553–597. <https://doi.org/10.1002/qj.828>
- Emanuel K (2003) Tropical cyclones. *Annu Rev Earth Planet Sci* 31:75–104. <https://doi.org/10.1146/annurev.earth.31.1.1090>
- Emanuel K, Nolan D (2004) Tropical cyclone activity and the global climate system. In: Proceedings of the 26th conference on hurricanes and tropical meteorology. American Meteorological Society, Miami, FL, pp 240–241
- Felton C, Subrahmanyam B, Murty V (2013) ENSO-modulated cyclogenesis over the Bay of Bengal. *J Clim* 26:9806–9818. <https://doi.org/10.1175/jcli-d-13-00134.1>
- Girishkumar M, Ravichandran M (2012) The influences of ENSO on tropical cyclone activity in the Bay of Bengal during October–December. *J Geophys Res Oceans* 117:C02033. <https://doi.org/10.1029/2011jc007417>
- Girishkumar M, Suprit K, Vishnu S, Prakash V, Ravichandran M (2014a) The role of ENSO and MJO on rapid intensification of tropical cyclones in the Bay of Bengal during October–December. *Theor Appl Climatol* 120:797–810. <https://doi.org/10.1007/s00704-014-1214-z>
- Girishkumar M, Thanga Prakash V, Ravichandran M (2014b) Influence of Pacific Decadal Oscillation on the relationship between ENSO and tropical cyclone activity in the Bay of Bengal during October–December. *Clim Dyn* 44:3469–3479. <https://doi.org/10.1007/s00382-014-2282-6>
- Gon Z, Wang P, Ma J (2002) Application of a simplified calculation scheme for mean meridional circulation mass stream function (in Chinese). *J Nanjing Inst Meteorol* 25:328–333. <https://doi.org/10.13878/j.cnki.dqkxxb.2002.03.006>
- Gray W (1968) Global view of the origin of tropical disturbances and storms. *Mon Weather Rev* 96:669–700. [https://doi.org/10.1175/1520-0493\(1968\)096%3c0669:GVOTO%3e2.0.CO;2](https://doi.org/10.1175/1520-0493(1968)096%3c0669:GVOTO%3e2.0.CO;2)
- Gray W (1985) Tropical cyclone global climatology. WMO Technical Document WMO/TD 72:3–19
- Hu C, Zhang C, Yang S, Chen D, He S (2017) Perspective on the northwestward shift of autumn tropical cyclogenesis locations over the western North Pacific from shifting ENSO. *Clim Dyn* 51:2455–2465. <https://doi.org/10.1007/s00382-017-4022-1>
- Jiang X, Zhao M, Waliser D (2012) Modulation of tropical cyclones over the Eastern Pacific by the intraseasonal variability simulated in an AGCM. *J Clim* 25:6524–6538. <https://doi.org/10.1175/jcli-d-11-00531.1>
- Kalnay E et al (1996) The NCEP/NCAR 40-year reanalysis project. *Bull Am Meteorol Soc* 77:437–472. [https://doi.org/10.1175/1520-0477\(1996\)077%3c0437:TNYRP%3e2.0.CO;2](https://doi.org/10.1175/1520-0477(1996)077%3c0437:TNYRP%3e2.0.CO;2)
- Kosaka Y, Nakamura H (2006) Structure and dynamics of the summertime Pacific–Japan teleconnection pattern. *Q J R Meteorol Soc* 132:2009–2030. <https://doi.org/10.1256/qj.05.204>
- Krishnamurthy L, Krishnamurthy V (2013) Influence of PDO on South Asian summer monsoon and monsoon–ENSO relation. *Clim Dyn* 42:2397–2410. <https://doi.org/10.1007/s00382-013-1856-z>
- Kurtzman D, Scanlon B (2007) El Niño–Southern Oscillation and Pacific Decadal Oscillation impacts on precipitation in the southern and central United States: evaluation of spatial distribution and predictions. *Water Resour Res*. <https://doi.org/10.1029/2007wr005863>
- Li Z, Yu W, Li T, Murty V, Tangang F (2013) Bimodal character of cyclone climatology in the Bay of Bengal modulated by monsoon seasonal cycle. *J Clim* 26:1033–1046. <https://doi.org/10.1175/jcli-d-11-00627.1>
- Liu K, Chan J (2013) Inactive period of Western North Pacific Tropical Cyclone activity in 1998–2011. *J Clim* 26:2614–2630. <https://doi.org/10.1175/jcli-d-12-00053.1>
- Mauw R (2011) Recent historically low global tropical cyclone activity. *Geophys Res Lett* 38:L14803. <https://doi.org/10.1029/2011gl047711>
- McBride J (1995) Tropical cyclone formation. Global perspective on tropical cyclones. World Meteorological Association, Geneva, pp 63–105
- Mohanty U, Mohapatra M, Singh O, Bandyopadhyay B, Rathore L (2013) Monitoring and prediction of tropical cyclones in the Indian Ocean and climate change. Springer Science and Business Media, New York
- Rayner N et al (2003) Global analyses of sea surface temperature, sea ice, and night marine air temperature since the late nineteenth century. *J Geophys Res Atmos* 108:4407. <https://doi.org/10.1029/2002jd002670>
- Shi N, Wang X, Zhang L, Xu H (2016) Features of Rossby wave propagation associated with the evolution of summertime blocking highs with different configurations over northeast Asia. *Mon Weather Rev* 144:2531–2546. <https://doi.org/10.1175/mwr-d-15-0369.1>
- Takaya K, Nakamura H (2001) A formulation of a phase-independent wave-activity flux for stationary and migratory quasigeostrophic eddies on a zonally varying basic flow. *J Atmos Sci* 58:608–627. [https://doi.org/10.1175/1520-0469\(2001\)058%3c0608:AFOAP%3e2.0.CO;2](https://doi.org/10.1175/1520-0469(2001)058%3c0608:AFOAP%3e2.0.CO;2)
- Wang P (1994) Diagnosis of mean meridional circulation of the model atmosphere in the GCM with low resolution vertically (in Chinese). *J Nanjing Inst Meteorol* 17:200–204. <https://doi.org/10.13878/j.cnki.dqkxxb.1994.02.012>
- Wang X, Liu H (2015) PDO modulation of ENSO effect on tropical cyclone rapid intensification in the western North Pacific. *Clim Dyn* 46:15–28. <https://doi.org/10.1007/s00382-015-2563-8>
- Wang L, Chen W, Huang R (2008) Interdecadal modulation of PDO on the impact of ENSO on the east Asian winter monsoon. *Geophys Res Lett* 35:L20702. <https://doi.org/10.1029/2008gl035287>
- Wang S, Buckley B, Yoon J, Fosu B (2013) Intensification of premonsoon tropical cyclones in the Bay of Bengal and its impacts

- on Myanmar. *J Geophys Res Atmos* 118:4373–4384. <https://doi.org/10.1002/jgrd.50396>
- Wang X, Wang C, Zhang L, Wang X (2015) Multidecadal variability of tropical cyclone rapid intensification in the Western North Pacific. *J Clim* 28:3806–3820. <https://doi.org/10.1175/jcli-d-14-00400.1>
- Wang C, Wang X, Weisberg R, Black M (2017) Variability of tropical cyclone rapid intensification in the North Atlantic and its relationship with climate variations. *Clim Dyn* 49:3627–3645. <https://doi.org/10.1007/s00382-017-3537-9>
- Webster P, Holland G, Curry J, Chang H (2005) Changes in tropical cyclone number, duration, and intensity in a warming environment. *Science* 309:1844–1846. <https://doi.org/10.1126/science.1116448>
- Wu R, Wang B (2002) A contrast of the East Asian summer monsoon–ENSO relationship between 1962–77 and 1978–93. *J Clim* 15:3266–3279. [https://doi.org/10.1175/1520-0442\(2002\)015%3c3266:ACOTEA%3e2.0.CO;2](https://doi.org/10.1175/1520-0442(2002)015%3c3266:ACOTEA%3e2.0.CO;2)
- Yanase W, Satoh M, Taniguchi H, Fujinami H (2012) Seasonal and intraseasonal modulation of tropical cyclogenesis environment over the Bay of Bengal during the extended summer monsoon. *J Clim* 25:2914–2930. <https://doi.org/10.1175/jcli-d-11-00208.1>
- Yang L, Chen S, Wang C, Wang D, Wang X (2017) Potential impact of the Pacific Decadal Oscillation and sea surface temperature in the tropical Indian Ocean–Western Pacific on the variability of typhoon landfall on the China coast. *Clim Dyn* 51:2695–2705. <https://doi.org/10.1007/s00382-017-4037-7>
- Yu B, Zwiers F (2007) The impact of combined ENSO and PDO on the PNA climate: a 1,000-year climate modeling study. *Clim Dyn* 29:837–851. <https://doi.org/10.1007/s00382-007-0267-4>
- Yu B, Zwiers F (2010) Changes in equatorial atmospheric zonal circulations in recent decades. *Geophys Res Lett* 37:L05701. <https://doi.org/10.1029/2009gl042071>
- Yu B, Zwiers F, Boer G, Ting M (2012) Structure and variances of equatorial zonal circulation in a multimodel ensemble. *Clim Dyn* 39:2403–2419. <https://doi.org/10.1007/s00382-012-1372-6>
- Zhao H, Wang C (2015) Interdecadal modulation on the relationship between ENSO and typhoon activity during the late season in the western North Pacific. *Clim Dyn* 47:315–328. <https://doi.org/10.1007/s00382-015-2837-1>
- Zhao H, Duan X, Raga G, Klotzbach P (2018) Changes in characteristics of rapidly intensifying Western North Pacific tropical cyclones related to climate regime shifts. *J Clim* 31:8163–8179. <https://doi.org/10.1175/jcli-d-18-0029.1>

Publisher's Note Springer Nature remains neutral with regard to jurisdictional claims in published maps and institutional affiliations.